Nanotechnology

Kinetic modeling of interfacial abruptness in axial nanowire heterostructures

To cite this article before publication: Egor Leshchenko *et al* 2022 *Nanotechnology* in press https://doi.org/10.1088/1361-6528/aca1c9

Kinetic modeling of interfacial abruptness in axial nanowire heterostructures

E. D. Leshchenko[1] and V. G. Dubrovskii[2]

[1] Submicron Heterostructures for Microelectronics, Research & Engineering Center, RAS, 26 Politekhnicheskaya, 194021, St. Petersburg, Russia

[2] Faculty of Physics, St. Petersburg State University, Universitetskaya Embankment 13B, 199034 St. Petersburg, Russia

E-mail: leshchenko.spb@gmail.com

Abstract

Kinetic modeling of the formation of axial III-V nanowire heterostructures grown by the Au-catalyzed vapor-liquid-solid method is presented. The method is based on a combination of kinetic growth theory for different binaries at the liquid-solid interface and thermodynamics of ternary liquid and solid alloys. Non-stationary treatment of the compositional change obtained by swapping material fluxes allows us to compute the interfacial abruptness across nanowire heterostructures and leads to the following results. At high enough supersaturation in liquid, there is no segregation of dissimilar binaries in solid even for materials with strong interactions between III-V pairs, such as InGaAs. This leads to the suppression of the miscibility gaps by kinetic factors. Increasing the Au concentration widens the heterointerface at low Au content and narrows it at high Au content in a catalyst droplet. The model fits quite well the data on the compositional profiles across nanowire heterostructures based on both group III and group V interchange. Very sharp heterointerfaces in double of InAs/InP/InAs nanowire heterostructures is explained by a reduced reservoir effect due to low solubility of group V elements in liquid.

Keywords: III-V nanowires, axial nanowire heterostructures, interfacial abruptness, modeling

1. Introduction

Nanowire (NW) heterostructures, particularly those based on III-V NWs [1, 2], have great potential in fundamental studies of physical properties of semiconductor nanomaterials as well as in laser [3], sensing [4] and solar energy harvesting [5] technologies. The main advantage of NWs over other nano-heterostructures is an almost unlimited degree of freedom in band structure engineering, provided by the possibility of combining lattice mismatched materials and modulating the chemical composition within a single NW [6, 7]. Thanks to the free-standing geometry of NWs, different binary materials can be stacked vertically in axial NW heterostuctures [8-10] or across the NW axis in core-shell NW heterostructures [11, 12]. Dislocation-free growth of III-V NWs on Si substrates and high crystal quality of NW heterostructures in highly mismatched material systems such as InAs/GaAs or InGaN/GaN are difficult to achieve in planar layers or nanostructures having smaller aspect ratios. Using NW heterostructures based on different III-V materials including nitrides (from wide gap GaN to narrow gap InSb) opens a path for Si-integrated III-V optoelectronics in a wide spectral range covering UV, visible, and IR bands. One of the most common ways to produce III-V NWs and III-V NW heterostructures is the vapor-liquid-solid (VLS) method [13], in which the NWs grow from supersaturated catalyst droplets fed from a gaseous phase (vapor in the case of metal organic chemical vapor deposition (MOCVD) [14]) or molecular beams in the case of molecular beam epitaxy (MBE) [15]). The catalyst droplet may either contain a foreign element which does not incorporate into NWs, or made of group III metals constituting the NW itself. The Au-catalyzed VLS growth of III-V NWs [16] remains predominant due to its versality in MOCVD and related epitaxy techniques. The second approach, called the self-catalyzed VLS growth [17], is often used in MBE to prevent the unwanted NW contamination with Au [18] and enhance the structural control over the NW ensembles grown in patterned arrays of pinholes in silica mask on Si substrates [19].

Despite the recent progress in fabrication and tuning the properties of III-V NW heterostructures, some issues still need to be resolved. The first problem arises from the nature of the VLS growth, in which the composition of a liquid droplet cannot be instantaneously changed by switching the vapor fluxes. Since the chemical composition of the droplet determines the composition of the NW, there is a gradual transition from one binary to the other in axial NW heterostructure. This reservoir effect [20] broadens the heterointerface and cannot be fully circumvented in the VLS growth mode. However, the interfacial abruptness can be enhanced by growth interruptions which decrease the number of group III atoms stored in the droplet [21], or by growing III-V heterostructures based on the interchange of highly volatile

group V species, such as InP/InAs/InP [22]. The second problem is the morphological control over the NW diameter and maintaining the droplet stability at the NW top [22-24]. Third, ternary III-V materials may spontaneously separate into core-shell structures [25, 26] or segregate inside a ternary NW due to the presence of thermodynamically forbidden miscibility gaps [27,28] without changing the composition of vapor.

There are three types of models for composition of ternary III-V NWs and NW heterostructures developed so far. The equilibrium models assume that the incorporation of pairs into the solid occurs under equilibrium between the liquid and solid phases [27]. They fully ignore the influence of the NW growth kinetics as the incorporation rates of different binaries tends to zero in such conditions. The nucleation-limited model [28] predicts the segregation of a solid solution into pure binaries for systems with high lattice mismatch such as InGaAs or InGaN. This feature is due to the fact that the nucleation model describes the composition of the critical nucleus rather than growth of the full NW monolayer. Suppression of the miscibility gap may be described by introducing a compositional-dependent surface energy [29], but more generally by including the kinetic factors of the NW growth [30]. Finally, kinetic models [31] present a simplified growth picture considering the mass balance and irreversible growth rates of different binaries, which are not influenced by the interactions in the droplet and solid NW.

Consequently, here we present a growth model for the Au-catalyzed and self-catalyzed axial III-V NW heterostructures which combines the kinetic and thermodynamic factors. Our approach generalizes some ideas used previously in Refs. [21], [30], [32] and [33]. The dependence of the ternary NW composition on the liquid content is obtained using the kinetic model of Ref. [32] which treats the growth process in terms of composition-dependent incorporation rates of different binaries. We develop this approach by linking the mass balance in the droplet to the crystallization rates of different III-V pairs at the liquid-solid interface. Non-stationary treatment of the compositional change obtained by swapping material fluxes in vapor allows us to compute the compositional profiles and interfacial abruptness across NW heterostructures versus the material fluxes and droplet composition. The model fits quite well the data on the compositional profiles in axial NW heterostructures based on both group III and group V interchange, and should be useful for tuning the properties of NW heterostructures in a wide range of material systems.

2. Model

We consider an axial III-V NW heterostructure growing from liquid droplet resting at the NW top, as shown in Figure 1. The element U acts as an external catalyst (often Au), so atoms of type U remain in the droplet and do not incorporate into the solid NW. One should put its concentration to zero to describe the self-catalyzed VLS growth. The VLS growth starts with a binary BD material (say, InAs) NW forming from B (In) and D (As) vapor fluxes. To form a heterojunction, the flux of B atoms, V_B, is replaced by the flux of A atoms, V_A (say, Ga). This leads to the formation of a quaternary $ABDU$ liquid melt in the droplet and a ternary ABD NW. The number of B atoms in the droplet and NW decreases due to their absence in vapor. For Au-catalyzed VLS growth of axial InAs/GaAs NW heterostructures, quaternary liquid $ABDU$ is InGaAsAu and ternary NW is InGaAs, with composition x determined by the fraction of GaAs pairs in the ternary alloy.

The composition of each NW monolayer $A_xB_{1-x}D$ is determined by the content of AD pairs in solid, $x = N_{AD}/(N_{AD} + N_{BD})$, where N_{AD} and N_{BD} are the numbers of AD and BD pairs in the monolayer, respectively. When the incorporation of B atoms into the solid NW stops, a binary AD NW segment completes the formation of BD/AD axial NW heterostructure. The AD/BD junction of a double heterostructure can be obtained by the reverse replacement of the A flux.

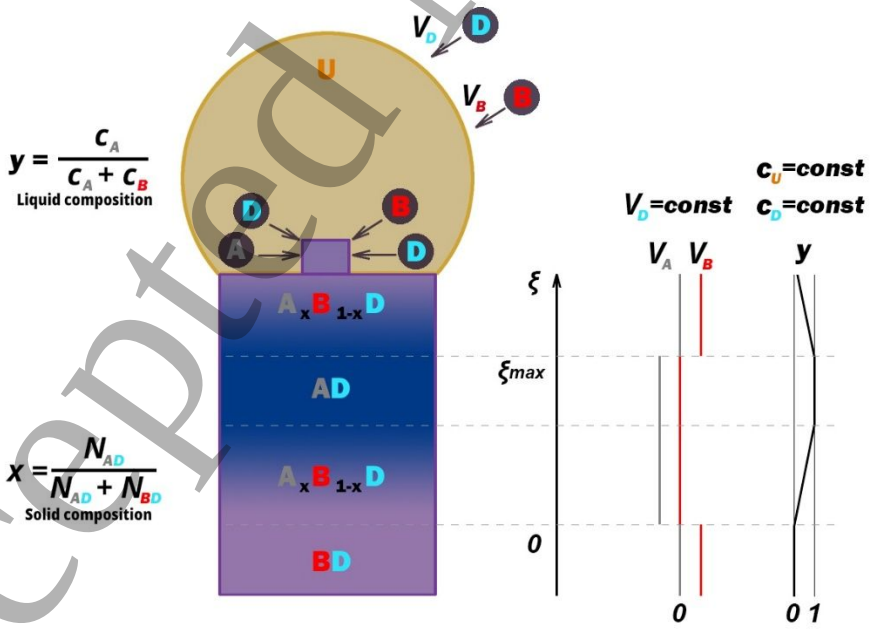

Figure 1. Schematic illustration of the double heterostructure formation in a VLS III-V NW.

The number A atoms in the droplet, N_A^L, changes in time due to the atomic influx V_A and the incorporation of AD pairs into the NW [21]

$$\frac{dN_A^L}{dt} = V_A - N_{III}^{ML} r x. \quad (1)$$

Here N_{III}^{ML} is the total number of AD and BD pairs in a NW monolayer and r is the NW elongation rate which is assumed independent of time. Introducing the axial coordinate, $\xi = rt$, Eq. (1) can be put

$$\frac{d\xi}{dx} = \frac{1}{ga - x} \frac{dy}{dx} c_{tot}. \quad (2)$$

Here, $a = {V_A}/{(N_{III}^{ML} r)}$ is the dimensionless atomic flux of the element A, and $c_{tot} = c_A + c_B$, with c_A and c_B being the concentrations of A and B atoms in liquid, respectively. The geometrical coefficient g is given by $g = N_{III}^{ML}/N_L$, with N_L being the total number of all atoms in the droplet, and depends on the NW radius and droplet contact angle [21,28]. The liquid composition y is given by the relative content of element A in the droplet, $y = {c_A}/{c_{tot}}$. The concentrations of D and U elements in the droplet (c_D and c_U, respectively) are constant during growth.

As for the incorporation of different pairs into solid, we consider the steady state growth of a ternary supercritical nucleus (one per monolayer), defined by the attachment and detachment rates of the two binaries. The incorporation rates of AD and BD pairs into the solid state can be written as $dN_{AD}/dt = W_{AD}\left(1 - e^{-\Delta\mu_{AD}}\right)$ and $dN_{BD}/dt = W_{BD}\left(1 - e^{-\Delta\mu_{BD}}\right)$, with the corresponding attachment rates $W_{AD} = K_{AD} c_A c_D$ and $W_{BD} = K_{BD} c_B c_D$ [32]. Here K_{AD} and K_{BD} are the crystallization rates which summarize the kinetic growth effects. The $\Delta\mu_{AD} = \mu_A^l + \mu_D^l - \mu_{AD}^s$ and $\Delta\mu_{BD} = \mu_B^l + \mu_D^l - \mu_{BD}^s$ are the chemical potential differences per III-V pair between the liquid alloy (labelled "l") and solid binaries AD and BD (labelled "s"), respectively. These chemical potentials are expressed in thermal units. The steady state solid composition $x = (dN_{AD}/dt)/(dN_{AD}/dt + dN_{BD}/dt)$ can be then obtained as a function of the liquid composition in the from

$$x = \frac{1}{1 + \frac{(1-y)}{y} k \frac{\left(1 - e^{-\Delta\mu_{BD}}\right)}{\left(1 - e^{-\Delta\mu_{AD}}\right)}}, \quad (3)$$

with $k = K_{BD}/K_{AD}$.

The chemical potential of species $\alpha = (A,B,D)$ in the liquid phase can be expressed as sum of the chemical potential in the pure liquid μ_α^0, the configuration entropy of mixing, and the interaction term φ_α according to $\mu_\alpha^l = \mu_\alpha^0 + \ln c_\alpha + \varphi_\alpha$ [27-29,31,32]. For the φ_α terms, we use the regular solution model with the interaction parameters given by the Redlich–Kister polynomials [32]. More details are given in the Supporting Information (SI). The chemical potentials of AD and BD pairs in solid are given by $\mu_{AD}^s = \mu_{AD}^0 + \ln x + \omega_s(1-x)^2$ and $\mu_{BD}^s = \mu_{BD}^0 + \ln(1-x) + \omega_s x^2$, respectively. Here, μ_{AD}^0 and μ_{BD}^0 are the chemical potentials of pure AD and BD solid binaries, and ω_s is the pseudo-binary interaction parameter [28]. All the used values for the chemical potentials of pure liquids and solids, and different interaction parameters can be found in the SI. Substitution of these chemical potentials into Eq. (3) yields our final result for the liquid composition

$$y = \frac{x}{(1-x+kx)}\left(k + (1-x)\frac{e^{\psi_1}e^{\omega_s(1-x)^2} - ke^{\psi_2}e^{\omega_s x^2}}{c_D c_{tot}}\right), \quad (4)$$

with $\psi_1 = (\mu_{AD}^0 - \mu_A^0 - \mu_D^0) - (\varphi_A + \varphi_D)$ and $\psi_2 = (\mu_{BD}^0 - \mu_B^0 - \mu_D^0) - (\varphi_B + \varphi_D)$. Now, one should find the derivative dy/dx, substitute it into Eq. (2) and integrate it. No analytical integration is possible due to the presence of the exponential terms $e^{\omega_s(1-x)^2}$ and $e^{\omega_s x^2}$ in Eq. (4). Hence, our further analysis is based on numerical calculations. The control parameters of the model include thermodynamic constants such as chemical potentials of pure binaries and interaction terms, as in Refs. [27,28], and kinetics constants a and k which account for the NW growth dynamics [21,32].

3. Results and discussion

We first consider the interfacial abruptness of axial InAs/GaAs NW hererostructure depending on the As concentration c_{As} in an InGaAsAu droplet. We use $c_{Au} = 0.1$, $a = 3$, $g = 0.001$, and $k = 1$, at a temperature of 400 °C. The selected value of g corresponds to a NW radius R of 40 nm and a droplet contact angle β of 135°. Figure 2 shows the GaAs content x as a function of distance along the NW axis (the heterostructure height), measured in monolayers (MLs) (vertical distance divided by the ML height). It is seen that the As concentration influences very significantly the interfacial abruptness, while this dependence is almost absent in the nucleation-limited model [28]. Within our model, low values of c_{As} yield the miscibility gap, while at $c_{As} > 0.002$ the interface becomes continuous. Suppression of the miscibility gap occurs due the kinetic factors. Indeed, the contribution of the $e^{\omega_s(1-x)^2}$ and $e^{\omega_s x^2}$

terms in Eq. (4), which are responsible for the van-der-Waals loops, becomes weaker for larger $c_{As} = c_D$. Increasing the As concentration leads to wider heterointerfaces. Γ-shaped compositional profile at very low c_{As} transitions to an almost linear increase of the GaAs with the distance ξ at large enough c_{As}. A contour plot of the GaAs content in the InAs/GaAs NW heterostructure NW versus distance and As concentration in the droplet is given the SI (Figure S1).

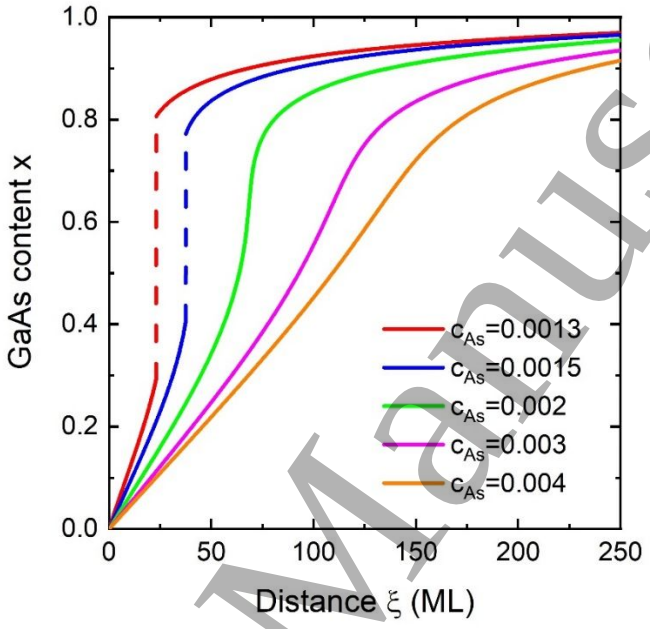

Figure 2. Compositional profiles across the InAs/GaAs NW heterostructures at different As concentrations in the droplet shown in the legend. The nanostructure height ξ is measured in MLs. The dashed sections of the curves correspond to the miscibility gaps.

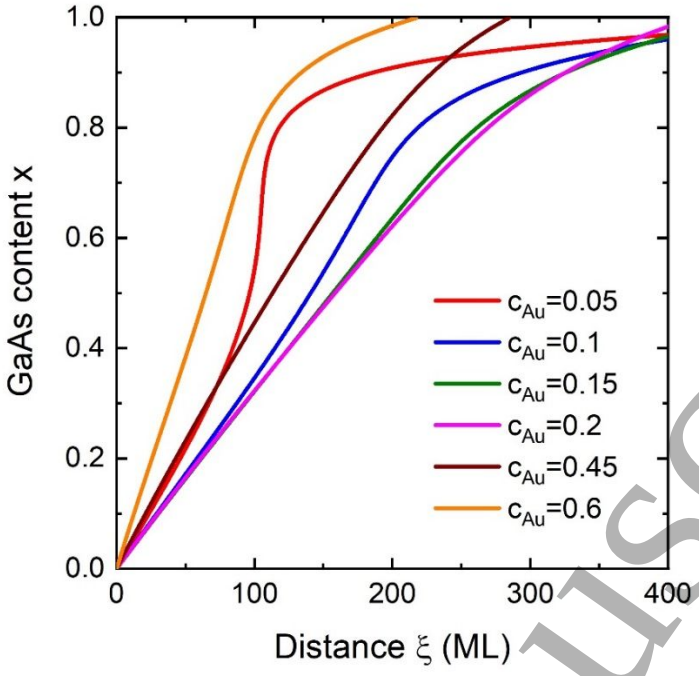

Figure 3. Composition profiles across the InAs/GaAs NW heterostructures at different Au concentrations in the droplet shown in the legend.

Next, we analyze the influence of the Au concentration in the droplet c_{Au} on the interfacial abruptness of the same InAs/GaAs NW heterostructure. We use $c_{As} = 0.0025$, $a = 2.5$, $g = 0.001$, and $k = 1$, at a temperature of 370 °C. Figure 3 shows the non-monotonic behavior of the interfacial abruptness with c_{Au}. Increasing the Au concentration from 0.05 (which is very close to self-catalyzed VLS growth without any Au in the droplet) to 0.2 broadens the heterointerface and changes its shape from Γ-shaped at $c_{Au} = 0.05$ to almost linear at $c_{Au} = 0.2$. Conversely, increasing c_{Au} from 0.2 to 0.6 sharpens the heterointerface, with changing its shape from almost linear to highly non-linear (but different from Γ-shaped curve at $c_{Au} = 0.05$) for the highest $c_{Au} = 0.6$. This interesting behavior can be explained by the competition between the two factors. First, the Au concentration influences the solid-liquid compositional dependence $x(y)$. In particular, an increase in the Au concentration leads to an increase of the In content in solid at a fixed liquid composition y (at least up to $c_{Au} = 0.5$). Thus, the derivative dy/dx increases in the compositional range employed for calculations. This results in an increase of $d\xi/dx$ and hence in an increase of the interfacial width. Second, the Au concentration is involved into the mass balance due to $c_{tot} = 1 - c_{Au}$. Consequently, the derivative $d\xi/dx$ decreases with the Au concentration and the interfacial abruptness improves. In the competition of these two opposite trends, the first one dominates at low enough Au

concentrations and the heterointerface is broadened, while it is narrowed at $c_{Au} > 0.2$ due to the dominant contribution of the second factor. It is noteworthy that the Γ-shaped compositional profile at a low Au content of 0.05 makes it difficult to grow the pure GaAs NW section, while at higher Au contents the pure GaAs should be achieved relatively quickly. A contour plot of the GaAs content in the InAs/GaAs NW heterostructure NW versus distance and Au concentration in the droplet is given the SI (Figure S2).

Figure 4 shows how the increase of the dimensionless atomic flux a results in sharper InAs/GaAs heterointerfaces. The curves were obtained at $c_{As} = 0.0017$, $c_{Au} = 0.2$, $g = 0.001$, and $k = 1$, at a temperature of 450 °C. This effect is simply explained by a faster feeding of the droplet with Ga, resulting in a faster replacement of In with Ga in both liquid and solid phases. In all cases, the reverse transition of GaAs to InAs is sharper than the direct transition from InAs to GaAs. A contour plot of the GaAs content in the InAs/GaAs NW heterostructure NW versus distance and the atomic flux a is given the SI (Figure S3).

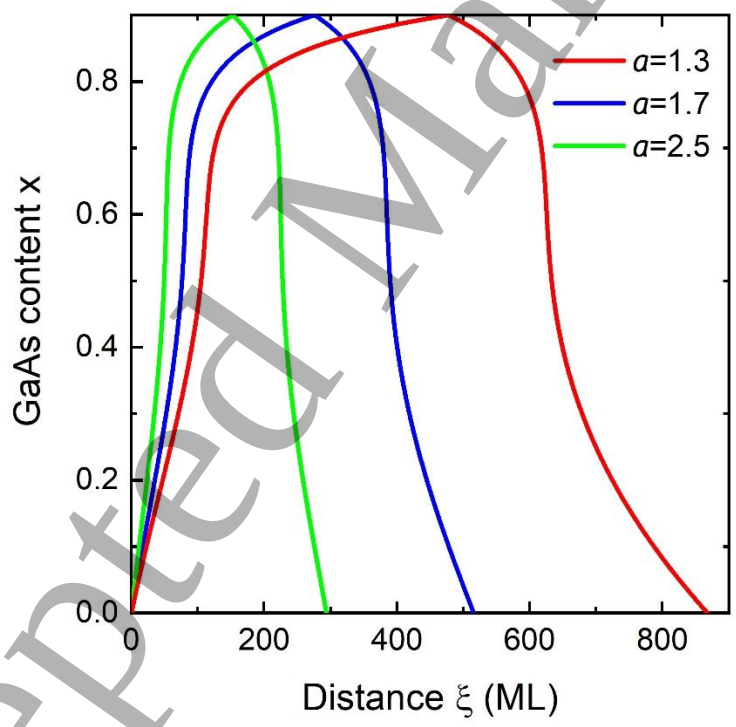

Figure 4. Composition profiles across the double InAs/GaAs/InAs NW heterostructures at different values of the atomic flux a shown in the legend.

4. Theory and experiment

Axial InAs/GaAs NW heterostructures of Ref. [20] were grown by Au-catalyzed MOCVD at 10 kPa with H_2 carrier gas flow of 13 L/min. Au aerosol seed particles with various diameters from 20 to 90 nm were deposited onto InAs (111)B substrates, yielding the diameters of the NW tips from 15 to 85 nm. The growth temperatures were varied from 380 to 470 °C. The growth was initiated by introducing trimethylindium (TMIn), and heterostructures were formed by turning off TMIn, flushing up to 30 s in AsH_3, and then turning on trimethylgallium. The InAs/GaAs interfacial abruptness scaled linearly with the NW diameter. The interfaces obtained with this simple procedure were found quite broad, as shown in Figure 5 for a 60 nm diameter NW grown at 470 °C. For this NW diameter, the gradient length is in the order of 150 monolayers. To convert the vertical distance to MLs, we divided the distance by the ML height $h(x) = xh_{GaAs} + (1-x)h_{InAs}$. Here, $h_{GaAs} = a_{GaAs}/\sqrt{3}$ and $h_{InAs} = a_{InAs}/\sqrt{3}$ are the GaAs and InAs monolayer heights, respectively, while $a_{GaAs} \approx 0.565$ and $a_{InAs} \approx 0.606$ are the lattice constants of GaAs and InAs, respectively. The interface gradient was found almost independent on the growth temperature. However, the interfaces were substantially sharpened by pulsing the Ga source during heterostructure formation to reduce the reservoir effect.

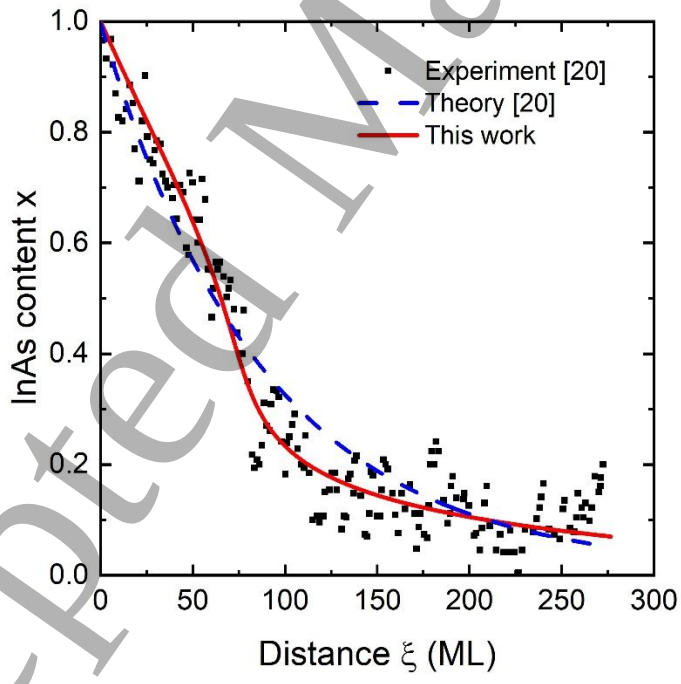

Figure 5. Experimental data on the compositional profile in 60 nm diameter InAs/GaAs NW heterostructure grown by Au-catalyzed MOCVD at 470 °C (symbols) [20], fitted by the model (line). The dashed blue line shows the exponential fit of Ref. [20]. The red curve is obtained from Equations (2) and (3).

The line in Figure 5 shows the fit to the data obtained from our model with $c_{Au} = 0.18$, $T = 470$ °C, $g = 0.00143$, corresponding to the experimental conditions, using the fitting parameters $c_{As} = 0.0033$ and $a = 1.9$. It is seen that the model reproduces very well the compositional profile, with a plausible As concentration which is generally beyond the detection limit. This fit is better than the simple exponential curve used in Ref. [20], shown by the dashed blue line in Figure 5. The compositional profile follows a law which seems more complex than exponential. A detailed comparison with the model of Ref. [20] is presented in the SI. Furthermore, it has been noticed in Ref. [20] that the extracted value of the diffusivity through the metal particle, used as the only fitting parameter, is 8 orders of magnitude lower than the typical diffusion coefficients in liquid. The growth temperature is much lower than the critical temperature of 543 °C for InGaAs solid alloy [28]. However, the GaAs content in the InGaAs gradient region changes monotonically from zero to unity according to the data. We can thus conclude that the miscibility gap within the gradient region is suppressed by the kinetic factors, as suggested by our model.

Double InAs/InP/InAs NW heterostructures of Ref. [22] were grown by Au-catalyzed chemical beam epitaxy (CBE) on InAs(111)B substrates by the Au-catalyzed VLS mechanism, using trimethylindium (TMIn), tert-butylarsine (TBAs), and tert-butylphosphine (TBP) as metalorganic precursors. The growth was started with InAs NW stems using constant TMIn and TBAs fluxes at a temperature of 430 °C. Then, to obtain InAs−InP NW heterojunction, the InP growth was carried out on the InAs stems at the same temperature using different combinations of TMIn and TBP fluxes. After that, the procedure was reversed to grow InP-InAs heterojunction. Special care was taken to ensure the droplet stability at the top of InP segments, which was only possible at a low TMIn flow of 0.1 Torr and a high TBP flow of 2.2 Torr. These parameters yielded a low In/Au ratio in the droplet of 1.3, a droplet contact angle of 104°, constant NW diameter and pure wurtzite crystal phase of both materials. Figure 6 shows that the interfacial abruptness in the optimized NW heterostructures was very sharp, in the order of a few monolayers. To convert the vertical distance to MLs, we divided the distance ξ by the InP monolayer height $h_{InP} = a_{InP}/\sqrt{3}$. This is possible because the lattice constants of InP and InAs are approximately the same ($a_{InP} \approx 0.587$ and $a_{InAs} \approx 0.606$).

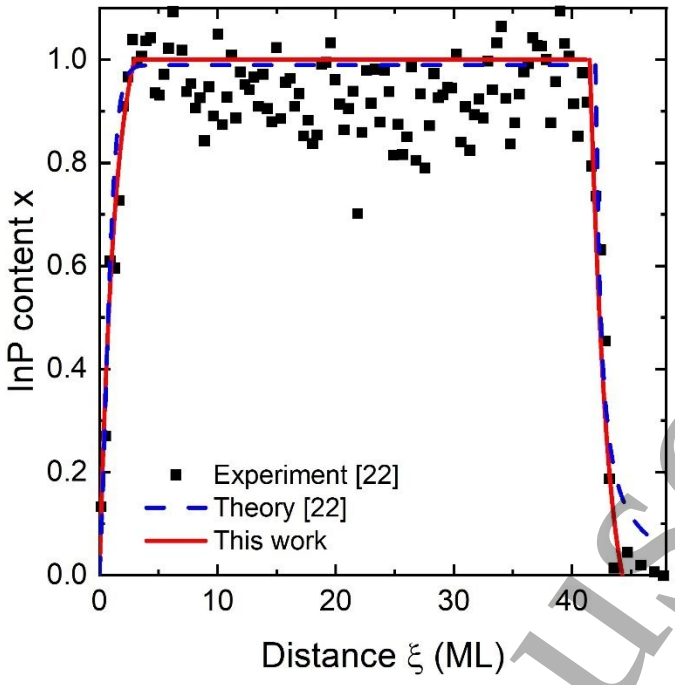

Figure 6. Experimental compositional profile across 40 nm diameter double InAs/InP/InAs heterostructure grown by CBE at 430 °C (symbols) [22], fitted by the model (line). The dashed blue line shows the modeling results of Ref. [22].

The line in Figure 6 shows the fit to the data obtained from our model with $T = 430$ °C, $c_{Au} = 0.43$, and $g = 0.005$, corresponding to the experimental conditions, using the fitting parameters $c_{tot} = 0.007$ and $a = 1.15$. The sharp interfaces are well reproduced within the model, and explained by an extremely low group V content in the droplet. Overall, this result shows again that axial NW heterostructures based on the group V interchange should generally be sharper than those based on the group III interchange due to a dramatically reduced reservoir effect [22,28,33]. Within the model of Ref. [22], a long tail is present at $x < 0.2$, which means that a large number of ternary monolayers (~15 MLs) is needed to achieve pure InAs binary. Our model predicts no such tail, which is also not seen experimentally. A more detailed comparison with the model of Ref. [22] is presented in the SI.

5. Conclusions

In conclusion, we have developed a model for the compositional profiles and interfacial abruptness in axial III-V NW heterostructures grown by the VLS method. The model takes into account the NW growth kinetics in terms of the alternating vapor fluxes, crystallization rates of different binaries at the liquid-solid interface, and thermodynamics of quaternary (ternary in the

case of self-catalyzed VLS growth) liquid and ternary solid alloys which manifest in the chemical potentials entering the governing equations. The model combines the approaches developed earlier in Refs. [21,27-33], which are applied to non-stationary VLS growth of axial NW heterostructures. It describes the transition from thermodynamically controlled to kinetically driven composition of NW heterostructures. The used assumptions of a time-independent NW growth rate and total concentration of the two elements intermixed in the droplet are not critical and will be refined in a later work. The droplet stability on the NW top [22], surface polarity [34], doping and other mesoscopic factors can also influence the NW heterostructure formation and require additional study. The model fits quite well the data on the compositional profiles in axial Au-catalyzed InAs/GaAs and InAs/InP/InAs NW heterostructures grown by different epitaxy techniques. The developed approach is not specific to III-V materials and can be generalized to include II-VI, oxide and hybrid NW heterostructures [35]. We considered the data on III-V NW heterostructures grown by VLS-MOCVD or CBE techniques. However, this method should work equally well for other CVD techniques and molecular beam epitaxy provided that the interchange of material influxes is much faster than the crystallization kinetics at the liquid-solid interface. The model and results should be useful for understanding the compositional trends in a wide range of NW heterostructures, tuning their properties to the desired values for different applications, and simulations of the NW-based optoelectronic device structures.

Acknowledgements

The authors thank Jonas Johansson (Lund University) for fruitful discussions. VGD gratefully acknowledges financial support of St. Petersburg State University under the research grant No. 93020138.

Conflicts of Interest

The authors declare no conflicts of interest.

References

[1] Hyun J K, Zhang S, and Lauhon L J 2013 Nanowire Heterostructures *Annu. Rev. Mater. Res.* **43** 21.1–21.29

[2] Johansson J and Dick K A 2011 Recent advances in semiconductor nanowire heterostructures *CrystEngComm* **13** 7175–7184

[3] Yan R, Gargas D and Yang P 2009 Nanowire photonics *Nature Photonics* **3** 569–576

[4] Patolsky F and Lieber C M 2005 Nanowire nanosensors *Materials Today* **8** 20-28

[5] Wallentin J *et al* 2013 InP nanowire array solar cells achieving 13.8% efficiency by exceeding the ray optics limit *Science* **339** 1057–60

[6] Ghasemi M, Leshchenko E D and Johansson J 2020 Assembling your nanowire: an overview of composition tuning in ternary III–V nanowires *Nanotechnology* **32** 072001

[7] Liu B *et al* 2017 Semiconductor Solid-Solution Nanostructures: Synthesis, Property Tailoring, and Applications *Small* **13** 1701998

[8] Wu Y, Fan R and Yang P 2002 Block-by-Block Growth of Single-Crystalline Si/SiGe Superlattice Nanowires *Nano Lett.* **2** 83–86

[9] Björk M T *et al* 2002 One-dimensional Steeplechase for Electrons Realized *Nano Lett.* **2** 87–89

[10] Gudiksen M S *et al* 2002 Growth of nanowire superlattice structures for nanoscale photonics and electronics *Nature* **415** 617–620

[11] Lauhon L J *et al* 2002 Epitaxial core–shell and core–multishell nanowire heterostructures *Nature* **420** 57–61

[12] Royo M *et al* 2017 A review on III–V core–multishell nanowires: growth, properties, and applications *J. Phys. D: Appl. Phys.* **50** 143001

[13] Wagner R S and Ellis W C 1964 Vapor–liquid–solid mechanism of single crystal growth *Appl. Phys. Lett.* **4** 89–90

[14] Joyce H J 2019 III-V Nanowires and Related Nanostructures *Metalorganic Vapor Phase Epitaxy (MOVPE)* ed Irvine S and Capper P (John Wiley & Sons Ltd.) pp 217-239

[15] Jabeen F, Rubini S and Martelli F 2009 Growth of III–V semiconductor nanowires by molecular beam epitaxy *Microelectronics J.* **40** 442–445

[16] Messing M E *et al* 2009 The use of gold for fabrication of nanowire structures *Gold Bulletin* **42** 172–181

[17] Krogstrup P 2010 Structural Phase Control in Self-Catalyzed Growth of GaAs Nanowires on Silicon (111) *Nano Lett.* **10** 4475–4482

[18] Fontcuberta i Morral A, Colombo C and Abstreiter G 2008 Nucleation mechanism of gallium-assisted molecular beam epitaxy growth of gallium arsenide nanowires *Appl. Phys. Lett.* **92** 063112

[19] Dubrovskii V G *et al* 2015 Self-Equilibration of the Diameter of Ga-Catalyzed GaAs Nanowires *Nano Lett.* **15** 5580–5584

[20] Dick K A *et al* 2012 Controlling the Abruptness of Axial Heterojunctions in III–V Nanowires: Beyond the Reservoir Effect *Nano Lett.* **12** 3200–3206

[21] Priante G *et al* 2016 Sharpening the Interfaces of Axial Heterostructures in Self-Catalyzed AlGaAs Nanowires: Experiment and Theory *Nano Lett.* **16** 1917–1924

[22] Zannier V *et al* 2018 Nanoparticle Stability in Axial InAs–InP Nanowire Heterostructures with Atomically Sharp Interfaces *Nano Lett.* **18** 167–174

[23] Li L *al* 2017 Near Full-Composition-Range High-Quality $GaAs_{1-x}Sb_x$ Nanowires Grown by Molecular-Beam Epitaxy *Nano Lett.* **17** 622–630

[24] Ek M *et al* 2013 Diameter Limitation in Growth of III-Sb-Containing Nanowire Heterostructures *ACS Nano* **7** 3668–3675

[25] Dubrovskii V G *et al* 2016 Origin of Spontaneous Core–Shell AlGaAs Nanowires Grown by Molecular Beam Epitaxy *Cryst. Growth Des.* **16** 7251–7255

[26] Sun W *et al* 2016 Spontaneous formation of core–shell GaAsP nanowires and their enhanced electrical conductivity *J. Mater. Chem. C* **3** 1745–1750

[27] Glas F 2017 Comparison of Modeling Strategies for the Growth of Heterostructures in III–V Nanowires *Cryst. Growth Des.* **17** 4785–4794

[28] Dubrovskii V G *et al* 2017 Understanding the composition of ternary III-V nanowires and axial nanowire heterostructures in nucleation-limited regime *Mater. Des.* **132** 400–408

[29] Leshchenko E D and Johansson J 2021 Surface energy driven miscibility gap suppression during nucleation of III–V ternary alloys *CrystEngComm* **23** 5284–5292

[30] Roche E *et al* 2018 Circumventing the miscibility gap in InGaN nanowires emitting from blue to red *Nanotechnology* **29** 465602

[31] Dubrovskii V G and Sibirev N V 2016 Factors influencing the interfacial abruptness in axial III-V nanowire heterostructures *Cryst. Growth Des*. **16** 2019–2023

[32] Leshchenko E D and Johansson J 2020 Role of Thermodynamics and Kinetics in the Composition of Ternary III-V Nanowires *Nanomaterials* **10** 2553

[33] Dubrovskii V G 2017 Understanding the vapor-liquid-solid growth and composition of ternary III-V nanowires and nanowire heterostructures *J. Phys. D: Appl. Phys*. **50** 453001

[34] Sahoo P *et al*. 2012 Role of surface polarity in self-catalyzed nucleation and evolution of GaN nanostructures *Cryst. Growth Des.* **12** 2375

[35] Bansal S *et al* 2020 A highly efficient bilayer graphene/ZnO/silicon nanowire-based heterojunction photodetector with broadband spectral response *Nanotechnology* **31** 405205